Revealing Nanoscale Confinement Effects on Hyperbolic Phonon Polaritons with an Electron Beam

Andrea Konečná, Jiahan Li, James H. Edgar, F. Javier García de Abajo, Jordan A. Hachtel**

Dr. A. Konečná
Central European Institute of Technology, Brno University of Technology,
Brno, 612 00, Czech Republic
E-mail: andrea.konecna@vutbr.cz

Dr. A. Konečná and Prof. F.J. García de Abajo
ICFO-Institut de Ciencies Fotoniques, The Barcelona Institute of Science and Technology,
Castelldefels (Barcelona), 08860, Spain

Mr. J. Li and Prof J.H. Edgar
Tim Taylor Department of Chemical Engineering, Kansas State University, Manhattan, Kansas 66506, United States of America

Prof. F.J. García de Abajo
ICREA-Institució Catalana de Recerca i Estudis Avançats, Passeig Lluís Campanys 23,
Barcelona, 08010, Spain

Dr. J.A. Hachtel
Center for Nanophase Materials Sciences, Oak Ridge National Laboratory, Oak Ridge,
Tennessee, 37831, United States of America
E-mail: hachtelja@ornl.gov

Keywords: 2D materials, optoelectronics, hyperbolic phonon polaritons, hexagonal boron nitride, infrared spectroscopy, monochromated electron energy-loss spectroscopy, nanophotonics

Abstract: Hyperbolic phonon polaritons (HPhPs) in hexagonal boron nitride (hBN) enable the direct manipulation of mid-infrared light at nanometer scales, many orders of magnitude below the free-space light wavelength. High-resolution monochromated electron energy-loss spectroscopy (EELS) facilitates measurement of excitations with energies extending into the mid-infrared while maintaining nanoscale spatial resolution, making it ideal for detecting HPhPs. The electron beam is a precise source and probe of HPhPs, which allows us to observe nanoscale confinement in HPhP structures and directly extract hBN polariton dispersions for both modes in

the bulk of the flake and modes along the edge. Our measurements reveal technologically important non-trivial phenomena, such as localized polaritons induced by environmental heterogeneity, enhanced and suppressed excitation due to two-dimensional interference, and strong modification of high-momenta excitations such as edge-confined polaritons by nanoscale heterogeneity on edge boundaries. Our work opens exciting prospects for the design of real-world optical mid-infrared devices based on hyperbolic polaritons.

Notice: This manuscript has been authored by UT-Battelle, LLC, under Contract No. DE-AC0500OR22725 with the U.S. Department of Energy. The United States Government retains and the publisher, by accepting the article for publication, acknowledges that the United States Government retains a non-exclusive, paid-up, irrevocable, world-wide license to publish or reproduce the published form of this manuscript, or allow others to do so, for the United States Government purposes. The Department of Energy will provide public access to these results of federally sponsored research in accordance with the DOE Public Access Plan (http://energy.gov/downloads/doe-public-access-plan).

1. Introduction

Localized plasmon- and phonon-polaritons can be used to confine and manipulate light in the visible and near-infrared spectral regimes at the nanoscale.[1–3] The less developed mid-infrared (mid-IR) range holds great potential for new applications,[4–6] but is still limited by the lack of suitable materials systems for controlling low-energy excitations. Hexagonal boron nitride (hBN) is one such material, which, due to its dielectric anisotropy, possesses two Reststrahlen bands that support hyperbolic phonon polaritons (HPhPs) that confine mid-IR light to nanometer scales and allow it to propagate over micron-scales.[7,8] As a result, hBN can be combined with engineered nanopatterning as well as hybridization with other materials to enable a wide range of powerful nanophotonic devices.[9–15]

Only recently have optical analysis techniques achieved the spatial-resolution necessary to access HPhPs directly at the nanoscale. Scanning near-field optical microscopy (SNOM) is extensively used to probe the localization and dispersions of HPhPs at nano-length-scales,[16] and for studying other types of mid-IR light/matter interactions[17,18] in polaritonic nanostructures, heterostructures, and metamaterials.[19–22] However, the spatial resolution of SNOM is typically limited to a few tens of nanometers due to the size of the probe tip. Recently, electron energy-loss spectroscopy (EELS) in the scanning transmission electron microscope (STEM) has emerged as an alternative, more precise technique, as it can access the mid-IR excitations with sub-Ångstrom spatial resolution and as low as 3 meV (24 cm^{-1}) spectral resolution.[23–25] The electron beam can access a number of low-energy excitations including localized phonon modes,[26–29] molecular vibrations,[30–33] and the HPhPs.[34–36] Moreover, the precise control of the probe enables on-demand excitation of polarization-dependent modes,[37] directly induced localized quasiparticle coupling,[38–40] and measurements of polariton dispersions.[36,41–43]

Consequently, while EELS lacks the spectral resolution of SNOM, it possesses a key advantage in terms of spatial resolution, since the geometry of the tip and the sample fundamentally limit the maximum achievable resolution in SNOM. Beyond spatial resolution, monochromated EELS has several other benefits. For instance, in EELS the spectral axis is recorded in parallel (as opposed to serially) enabling fast acquisition of hyperspectral datasets at a far denser sampling of vibrational frequencies to more comprehensively characterize the polaritonic response.[44] Moreover, while high harmonics can push the maximum potential spatial-resolution of SNOM to < 10 nm values[45], the measurement and its interpretation are made more complex by the interaction of the tip and the sample. The converged electron probe is far-less sensitive to surface topographies/defects and sample geometries, and its sub-Ångstrom spatial-resolution is not sample-dependent. These factors combine to make monochromated EELS a powerful complement to SNOM, one that is extremely versatile and capable of expanding on relevant types of accessible samples for comprehensive nanoscale-resolved IR nanospectroscopy characterization.

Here, we discover several unique aspects of the nanoscale polaritonic response in hBN nanostructures by spectrally imaging HPhPs using monochromated STEM-EELS. A key property of HPhPs is geometrical confinement, and therefore, we examine the distinction between (1) HPhPs confined to the bulk of an exfoliated hBN flake and (2) HPhPs confined to the edge. Edge polaritons have been identified using EELS[36] and their dispersion measured by SNOM,[46] but here we additionally provide an EELS dispersion measurement of the edge polariton. The use of EELS is critical, as the high-spatial-resolution of the STEM accesses the high-wave-vector range of the edge polariton dispersion, revealing an extreme sensitivity to morphology of the flake wall. In addition, we find localization of polariton modes induced by

either material contacting the surface of the hBN flake and the flake geometry itself. For all of our measurements, we carefully model the behavior of the polaritons using idealized systems and demonstrate that nanoscale heterogeneity in the sample is responsible for the formation of the localized polariton modes.

2. Results and Discussion

A key aspect of the EELS analysis is that the beam is both the source and the probe, enabling control of excitations through beam positioning. **Figure 1** illustrates how the probe position on and around an ~18 nm thick hBN flake changes the excitation of HPhPs and the EEL spectra. Panels in Figure 1a-i show simulations of the electrostatic potential associated with the polariton excitation at 180 meV, 185 meV, and 190 meV (corresponding to 1451 cm^{-1}, 1492 cm^{-1}, and 1532 cm^{-1}, respectively) for probe positions 100 nm outside the flake, at the flake edge, and 100 nm inside the flake at each of these three mode energies. For all probe positions and energies the beam excites polaritons that propagate into the flake in all directions, as well as along the edge, even when the beam does not directly intersect the flake due to the 'aloof' effect.[47] The primary difference between probe positions is the relative intensity of the bulk vs. edge excitation, and the primary difference between energies are the wavelengths of the excitations in the flake. Note that at all energies the wavelength of the edge excitation is visibly shorter than that of the bulk excitation.

These effects manifest in the EELS line profile of an hBN flake edge. A high-angle annular-dark-field (HAADF) image of a flake edge is shown in Figure 1j, with the EEL line profile in Figure 1k (flake thickness ~12 nm). The EELS has a peak at ~176 meV (1419 cm^{-1}) that is excited everywhere, corresponding to the bulk polariton, but when the probe is close to the edge, excitations at even higher energy losses are observed, corresponding to the edge polariton.

Only when the probe is within ~10 nm of the edge of the flake is there a sufficiently strong excitation of the edge polariton to resolve it over the bulk-polariton signal, but, as illustrated in the simulations, it is still being excited at all probe positions. The high degree of localization of the edge polariton is surprising given that the aloof excitations are normally delocalized on the scale of hundreds of nm for comparable energies.[48] However, the result follows naturally from the high degree of confinement of the edge polariton to the flake edge, and the geometrical constraints on momentum transfer from the beam. When the beam is at the edge of the sample, it can transfer a large amount of momentum along the flake edge, enabling efficient excitation of the high-momentum (and hence high-energy-loss) branch of the polariton dispersions. Then, as the beam moves further away, only lower-momentum (lower-energy-loss) excitations are detected. The effect is most visible for the edge polariton, but it is also present in the aloof excitation of the bulk polariton, which continually redshifts as the probe moves further away from the sample (see **Figure S1**).

We also note that peaks at 160 meV and 200 meV (1290 cm^{-1} and 1613 cm^{-1}) are observed when the beam does intersect the flake, corresponding to the TO and LO phonons, respectively. These excitations are only accessed through impact scattering, and are not part of the polaritonic response, but they still play an important role, as they define the limits of the Reststrahlen band in which the HPhPs are active.

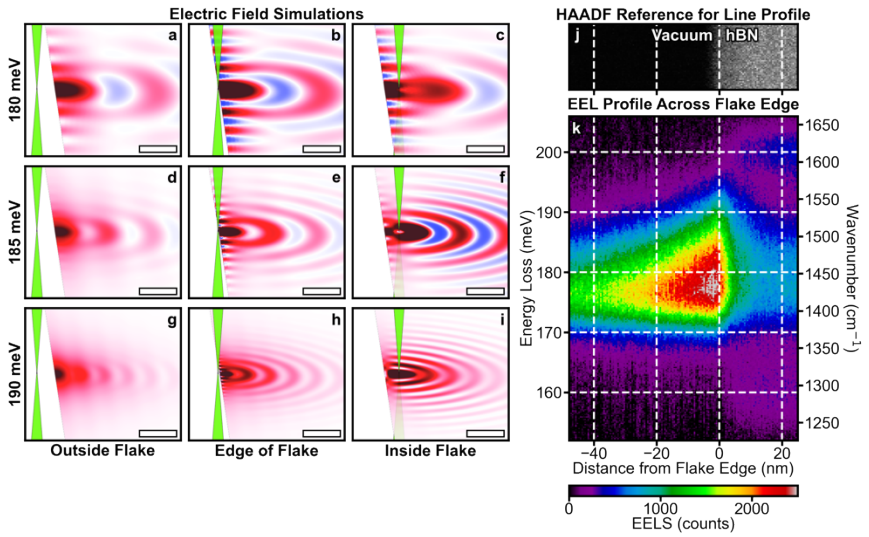

Figure 1. EELS Excitation of Hyperbolic Phonon Polaritons (HPhPs) at the Edge of an hBN Flake. (a-i) Electric field simulations of the polaritonic response in an hBN flake for different probe positions: 100 nm outside the flake (a,d,g), at the flake edge (b,e,h), and 100 nm inside the flake (c,f,i) at energy losses of 180 meV (1451 cm^{-1}) (a-c), 185 meV (1492 cm^{-1}) (d-f), and 190 meV (1532 cm^{-1}) (g-i). Scale bars = 200 nm. **(j)** HAADF reference image for line profile across hBN flake edge. **(k)** Measured EELS line profile across the edge of an 18 nm thick flake demonstrating highly localized excitation of the edge-confined polaritons.

The momentum selectivity afforded through careful probe positioning can go a step further to directly acquire HPhP dispersions with polariton interferometry.[34,36,41–43] This is exemplified for the bulk polariton dispersion in **Figure 2**. The experiment is shown schematically in Figure 2a: a line profile is acquired normal to the flake edge, in which polaritons that propagate directly towards the edge of the flake can reflect back resulting in interference. This is directly analogous to SNOM interferometry experiments, where the cantilevered tip is positioned at different distances away from the sample edge to isolate different polariton wavelengths and extract the dispersion.[16,18,19]

Such a line profile is plotted in Figure 2b, which shows that as the probe moves from deep (~200 nm) into the flake towards the edge, a dispersive peak corresponding to constructive interference with reflected polaritons emerges. As a result, each probe position approximately corresponds to a specific wavelength for which interference is maximized. Thus, by fitting the

peak energy as a function of distance from the edge, the entire dispersion is measured (see details of the fitting process expanded in Supporting Discussion 1).

The interference peaks also emerge in our numerical modeling. Figures 2c and 2d show the simulated EELS line profile, both broadened to match our experimental EELS energy resolution of 6 meV (c) and as directly obtained from the simulation (d). The broadened profile qualitatively and quantitatively matches with the EELS experiment, demonstrating that EELS accurately measures the bulk polariton interference. Note that both in the EELS experiment (Figure 2c) and in the simulation at EELS resolution (Figure 2c) the intensity on the high-energy side of the dispersive peak does not return to zero. The signal here corresponds to higher-order interference fringes, where instead of only completing one full period during propagation to the flake-edge and back, the polariton completes multiple periods. The full simulation (Figure 2d) clearly resolves many orders of these interference maxima, but only the first order peak can be individually identified at 6 meV energy resolution.

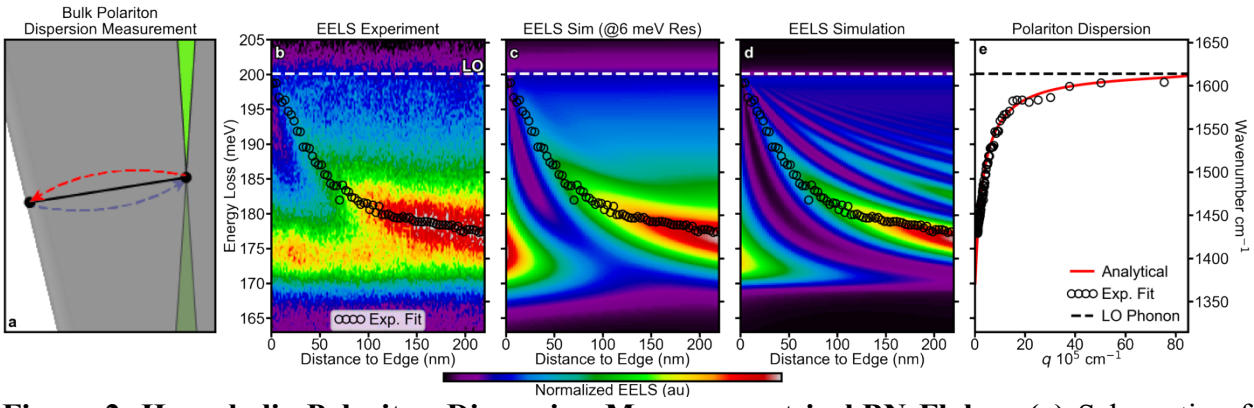

Figure 2. Hyperbolic Polariton Dispersion Measurement in hBN Flakes. (a) Schematic of polariton interferometry for a bulk HPhP dispersion measurement. Polaritons reflected from the edge create constructive interference at different wave vectors of the HPhP dispersion. **(b)** Experimental EELS line profile and fit of first-order interference peak (black circles). **(c,d)** Simulated EELS line profiles broadened to match the 6 meV experimental energy resolution (c) and at the native resolution of the calculation (d). **(e)** The dispersion is achieved by transforming the distance to the edge in the EELS measurement considering an edge-reflection phase $\phi_R = \pi/2$.

We compare the experimental dispersion to the analytical expression, showing good agreement out to high q values. (Flake thickness 12 nm).

We now transform the distances on the x axis of the interference peak to dispersion values, using the transformation $q = \frac{2\pi - \phi_R}{2x}$, where q is the polariton wave vector and ϕ_R is a reflection phase that is acquired by the polariton upon reflection. Here, we use $\phi_R = \frac{\pi}{2}$, which presents the best match between theory and experiment (**Figure S2** and Supporting Discussion 2). The transformed experimental dispersion is directly compared the analytical expression (Equation S1) in Figure 2e, achieving excellent agreement almost all the way out to 10^7 cm^{-1}.

We can also apply the same interferometry technique to measure the dispersion of edge-confined polaritons, as shown in **Figure 3**. Here, an aloof line profile is acquired moving along the edge of the flake (the same flake as from Figure 2) towards a sharp corner, enabling excited edge polaritons to propagate to the corner, reflect, and interfere with one another (see schematic in Figure 3a). The experimental and simulated (with and without broadening) EELS line profiles for the edge polariton are shown in Figure 3b-d, respectively, with the experimental fitted peak values plotted as black crosses in all three panels. While a dispersive peak is observed in both experiment and simulation, the agreement with theory here is far worse than it is for the bulk polariton in Figure 2.

Perhaps most importantly, the upper limit of the spectral intensity from the polariton excitation appears to be ~189 meV (1524 cm^{-1}), while it is at 195.2 meV (1574 cm^{-1}) in the simulations, corresponding to the energy of the high-q SO phonon.[34] Additionally, the EELS fits deviate from the simulated first-order peaks as the probe gets closer to the corner. The experimental dispersion is plotted in Figure 3e (using $\phi_R = \frac{3\pi}{4}$ for the transformation, see **Figure S3** and Supporting Discussion 2 for more details), and when compared to the analytical

expression (Equation S4), a significant deviation is observed. We attribute the effect to the nanoscale morphology of the edge wall. The above calculations treat the edge as a perfectly flat face, while real hBN flakes typically have significant heterogeneity and thickness variation along the edge. **Figure S4** in the Supporting Information shows several hBN flakes and demonstrates how the edge-wall morphology takes on a highly variable and heterogeneous character during the exfoliation process. The bulk HPhPs in the interior of the flake exist in a nominally uniform environment, but the edge HPhPs are confined directly to this heterogeneous region. Edge heterogeneity can be partly included in the simulations by changing the model system from a flat 90º wall to a tapered 45º wall to account for the step-like thickness gradient normally found in exfoliated flakes. Simulations of the *q*-resolved EELS probability of an excitation at a flat and tapered hBN flake edge are shown in Figures 3f and 3g, respectively. The flat edge probability exhibits high intensity directly along the analytical dispersion, but the tapered edge probability is both suppressed and redshifted from the analytical dispersion, especially at high-*q*, similar to the experiment.

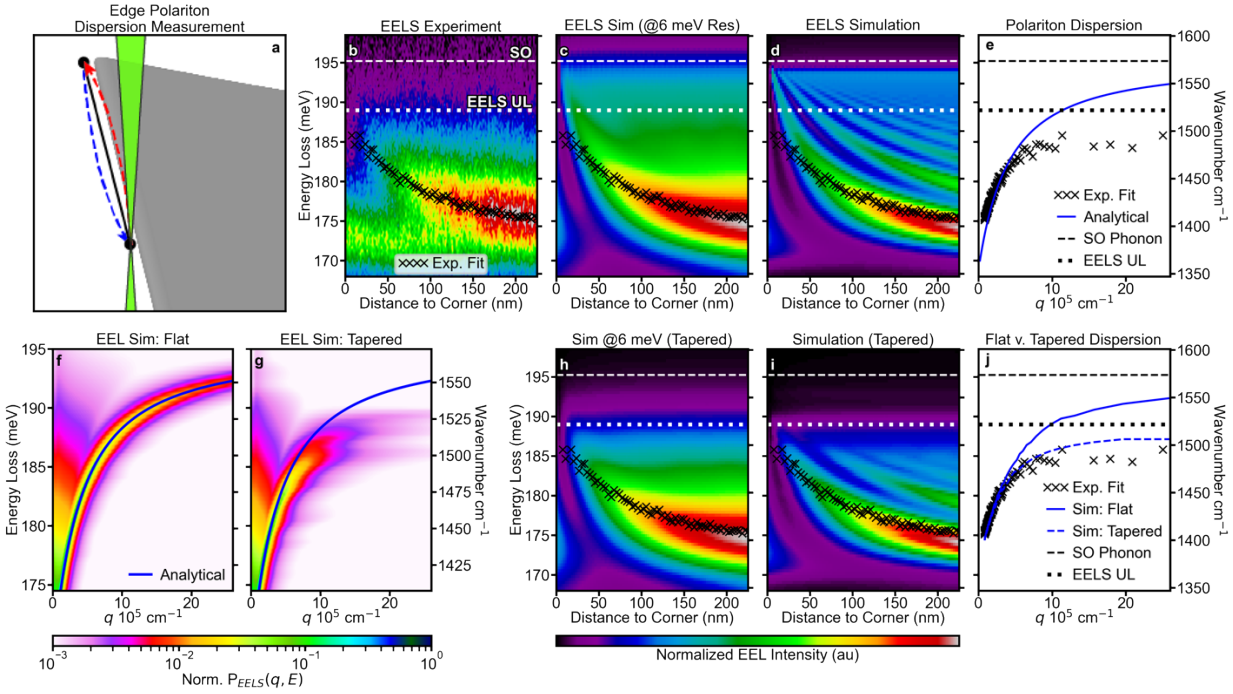

Figure 3. Polariton Dispersion Measurement at Heterogeneous Edges in hBN Flakes. (a) Schematic of polariton interferometry for an edge HPhP dispersion measurement. Polaritons reflected from the corner along the edge produced by HPhP interference. **(b-d)** Experimental and simulated EELS line profiles: experiment (b), spectrally broadened simulation to match EELS energy resolution (c), and the actual simulation (d). In (b-d), the upper limit of the measured EELS (at 189 meV, 1524 cm^{-1}) is marked with a dotted line and the theoretical upper limit (the SO phonon at 195.2 meV, 1574 cm^{-1}) is marked with a dashed line, demonstrating that measured and simulated EELS line scans have significantly different upper limits. **(e)** EELS dispersion transformed with a reflection phase $\phi_R = \frac{3\pi}{4}$, compared to the analytical expression for the edge polariton, exhibiting significant discrepancies. **(f,g)** Momentum-resolved EELS simulations for a 90º flat (f) and 45º tapered (g) edge, illustrating that high-q excitations are suppressed in the tapered edge (more closely resembling the excitations measured in the experimental line profile). **(h,i)** Broadened (h) and actual (i) line profiles simulated for a tapered edge flake, producing a much better match to the experimental upper limit. **(j)** Comparison of the experimental and simulated (for both flat and tapered edges) edge HPhP dispersions. The flake thickness is 12 nm.

The simulated (with and without broadening) EELS line profiles for the tapered edge are shown in Figures 3h and 3i. Here, the simulated and the experimental upper limit are in good agreement, and the fitted experimental peaks match the simulated first-order peak much more closely. The dispersions at the flat and tapered edge are determined by fitting the dispersive peaks in Figures 3c and 3h, respectively, and are compared to the experimental dispersion in Figure 3j. The flat-edge simulation replicates the analytical dispersion in Figure 3e, while the tapered-edge simulation is in excellent agreement with the experimentally retrieved dispersion. The comparison emphasizes the power of EELS as a complementary technique to SNOM. While the spatial variation of the dispersive peak is not significant and can be straightforwardly detected at the resolution of SNOM, it is the measurements within only a few nanometers of the flake edge where the real dispersion varies significantly from the analytical form. The spatial resolution of the STEM readily measures polaritons at this length scale, allowing us to reach far higher q values in a polariton interferometry measurement. Conversely, SNOM typically can only probe smaller q values $<10^6$ cm^{-1},[16,36,46] which is not sufficient to see the limiting behavior induced by the edge heterogeneity. However, as revealed by Figure 3e, the deviations between

the analytical and experimental edge polariton expressions only become significant above 10^6 cm^{-1}, necessitating the high-*q* interferometry in EELS with a well-defined focused probe.

The bulk polaritons can also be modified by subtle nanoscale environmental and geometric heterogeneity. In **Figure 4**, we consider the effect of materials contacting the surface of the hBN flakes. All our samples are supported on lacey carbon TEM grids, nominally thought to only support the flake and not influence the optical response substantially. However, hyperbolic polaritons are extremely sensitive to the surrounding environment,[41] and they can scatter and interact with the bordering region in a predictable manner.[49,50]. Thus, the lacey carbon that supports the flake also directly induces localized polariton modes in the flake. A schematic of our experiment is shown in Figure 4a. We find a hole in the lacey carbon underneath a large flake (far from the edges) and probe the hole region as a function of distance from the carbon edge (flake thickness ~8 nm). Figure 4b shows a HAADF image of the region used for the hyperspectral acquisition, centered around a ~400 nm diameter hole in the lacey carbon. For reference, the inset contains a low-magnification STEM image of the flake with the selected hole highlighted.

The hyperspectral dataset is partitioned into regions at different average distances *D* away from the carbon (i.e., the white ring in Figure 4b). We use 10 different distances (highlighted by different colors in Figure 4c) and plot the average EELS signal from each of them in Figure 4d. With no carbon/hBN interaction, the EELS signal would be uniform in all 10 regions, which is clearly not the case. The intensity of the bulk polariton peak increases by ~20% compared to the edge and it blueshifts slightly (173.3 meV to 174.6 meV or 1398 cm^{-1} to 1408 cm^{-1}). In addition, at the outmost region (*D*=13 nm) there is a shoulder at about 190 meV (1532 cm^{-1}), which redshifts to 185 meV (1492 cm^{-1}) for the *D*=51 nm region, and then further up towards the edge

of the dominant peak as the probe gets closer to the center of the hole. The effect can be understood by considering different pathways for polaritons excited by the beam: they can propagate past the carbon, or they can be reflected off it in analogy to the reflection observed at the edge of a disk. Thus, we describe the EELS signal as a combination of the two effects: infinite slab excitations (Figure 4e) and finite disk excitations (Figure 4f).

The calculated localized polariton modes of a 400 nm diameter finite hBN disk are plotted in Figure 4g. We detect multipole modes excited at the edge of the disk, breathing modes excited at the center, and *hybrid* modes emerging as combination of those two (analogous to localized surface plasmon modes[51,52]). We select finite-disk spectra to match the average D from the regions in Figure 4c, then add them to the infinite slab spectrum, and finally plot the combination in Figure 4h. The results after broadening with the 6 meV resolution of our microscope are plotted in Figure 4i.

The superposition of slab and disk excitations reproduces the major effects observed in the experiment, exhibiting enhanced intensity and a small blueshift of the peak energy at the center of the flake, which can now be attributed to the different localizations of the multipole and breathing modes. Moreover, Figure 4g shows that the *hybrid* modes have a dispersive change in energy as the probe gets closer to the edge, explaining the secondary position-dependent peak in the EELS data, which is also reproduced in the calculations. The localized disk modes can be further visualized using linear unmixing techniques as shown in **Figure S5** in the Supporting Information.

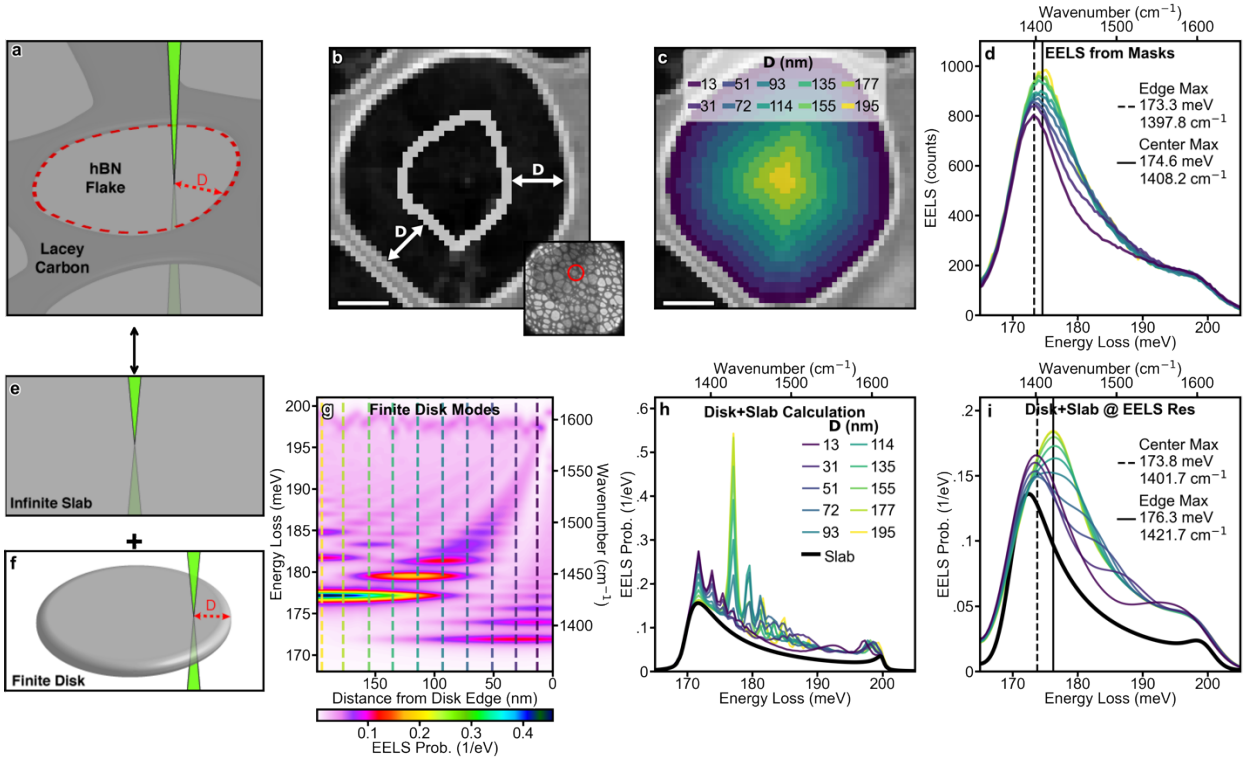

Figure 4. Localized Polariton Modes Induced by Environmental Heterogeneity. (a) Schematic of experiment to probe polariton interaction with supporting lacey carbon. **(b)** HAADF reference image of the region of interest. Inset: low-magnification STEM image of the entire hBN flake of thickness 8 nm with the hole marked in red. **(c)** Different regions of the selected hole in lacey carbon classified by the average distance *D* from carbon edge. **(d)** Spectra acquired from regions highlighted in (c). Scale bars = 100 nm. **(e,f)** Spectra in (d) can be described as a combination of the infinite slab response expected in the center of a large flake (e) with finite-disk-like modes induced by the lacey carbon (f). **(g)** Calculated modes for a finite hBN disk with 200 nm radius. *D* values from (c) and (d) are indicated through color-coordinated contours and lines. **(h)** Simulated EELS spectra for the same *D* values as in (c) and (d), obtained by combining the spectrum of an infinite slab signal (black) with the *D*-dependent disk modes (color). **(i)** Spectra in (h) broadened to match the EELS energy resolution, showing qualitative agreement with experiment in (d).

The geometry of the flake boundaries also has a dominant effect on the bulk polariton response. Here, we return to the flake used in Figures 2 and 3, which possessed a sharp corner, and acquire a hyperspectral image from the entire region (**Figure 5**). The probe interacts with both linear edges of the flake simultaneously, as shown schematically in Figure 5a. In Figure 5b-e, we show experimental energy-filtered EELS images for 0.5 meV wide windows centered at 180, 185, 190, and 195 meV (1452, 1492, 1532, and 1573 cm^{-1}), respectively, capturing the 2D

interference pattern at the hBN corner. The corresponding EELS simulations are shown in Figure 5f-i. The latter show a much larger degree of interference detail (especially at higher energies) compared to the experimental EELS with limited energy resolution. However, several key aspects of the interference patterns are still clearly discernable in the EELS experiment. Notably, interference minima forming dark fringes along the flake edges are observed in experiment and to exhibit similar width and energy dependence as the dark fringes in the simulations. The simulations also show higher-order interference minima and maxima deeper into the flake, increasing in number at the higher energies, although such interference is mostly blurred out at the 6 meV energy resolution of our EELS instrument. However, even these higher-order fringes are present in experiment under some circumstances: note that in both the 185 meV and 190 meV experimental images bright spots/fringes emerge from the positive interference. Additionally, the triangle-like geometry generates a localized-edge-polariton corner mode that is most pronounced in the 180 meV and 185 meV simulations as a bright spot on the edge of the flake (see further details in **Figure S6** and Supporting Discussion 3), while faint, comparable bright spots are present at the same position in the EELS image at 180 meV (see detectable features highlighted directly in **Figure S7**).

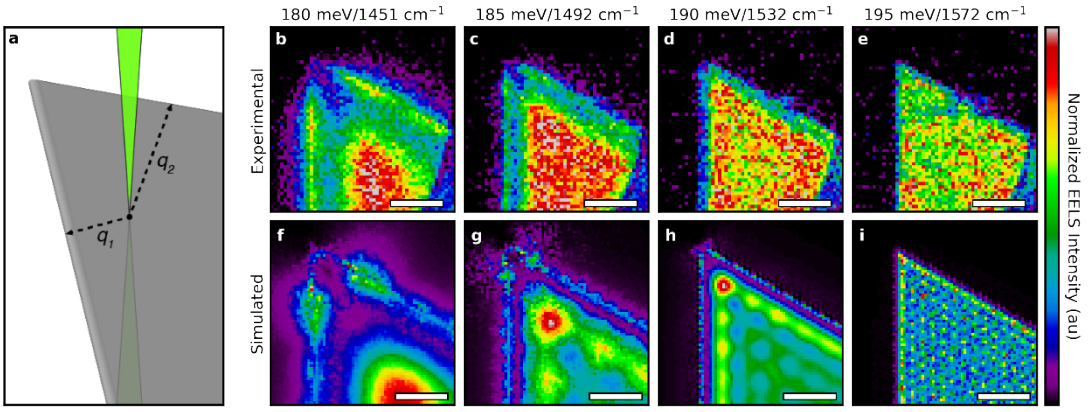

Figure 5. Phonon Polariton Mapping in the Corner of a hBN Flake. (a) Schematic of the experiment geometry. **(b-e)** Experimental measurements. **(f-i)** Simulations. The maps show the simultaneous existence of both bulk and edge HPhPs, producing both positive and negative

interference along the surface and at the edges, respectively, and a localized mode emerging close to the corner tip. Scale bars = 100 nm, flake thickness = 12 nm.

Lastly, it is important to note far away from the corner the signal is dominated by the interaction with the nearest edge. In contrast, close to the tip (within 100 nm) the polaritonic response is strongly influenced by both edges simultaneously and the full 2D geometry is needed to understand the response. This 2D interference is observed in the experiment almost as clearly as in the theory, demonstrating the ability of STEM-EELS to map constructive and destructive interference in nanostructured polaritonic materials.

3. Conclusion

We have revealed important characteristics of hyperbolic phonon polaritons in hBN flakes by controllably exciting and detecting these modes using a nanoscale electron probe. The polaritons are extremely sensitive to the surrounding environment and geometry, which enable us to probe a wide range of polariton properties including the dispersions of edge and bulk HPhPs, the emergence of localized modes induced by the surrounding environment and the flake geometry, and the presence of 2D interference patterns in nanostructured flakes. Our interferometry measurements show that, at high wave vector, nanoscale heterogeneity at the flake edge significantly modifies the real dispersion of the edge-confined polaritons, in a way that cannot be resolved by traditional infrared optical experiments. The bulk-confined polaritons are also highly sensitive to local nanoscale heterogeneity and can create 2D interference that suppresses or enhances the excitation of HPhPs at nano-length scales. Interaction of such heterogeneities within the material gives rise to localized modes determined by morphology. The combined use of aberration-correction and monochromation reduces the length scales that can be effectively characterized with interferometry, while it provides access to the high-q branch of

polariton dispersions and further allows us to rigorously characterize heterogeneity in the sample to reveal its influence on the polaritonic response. Furthermore, by using EELS, we can directly correlate signals across multiple energy regimes to compare the vibrational response (ultralow-loss regime), the electronic structure (low-loss regime), and the chemical composition (core-loss regime). Monochromated EELS elevates the potential design and understanding of nanophotonics in structured hBN flakes by providing precision control over both measurement and excitation of the nanoscale optical response to illuminate the innerworkings of complex photonics devices operating in the mid-infrared.

4. Methods

Sample Growth: hBN crystals were grown at atmospheric pressure from a molten iron-chromium solution using a ^{10}B isotopically enriched boron source.[53] Flakes were then chemically exfoliated and transferred onto lacey carbon TEM grids, where the flakes were only supported by the thin carbon web. The sizes of the flakes varied from tens of microns to tens of nanometers in diameter and a few layers to a few hundred nanometers in thickness. The flakes used in experiment were chosen as the ones with the most uniform thickness and cleanest edges, as determined from low magnification STEM imaging for monochromated EELS analysis.

STEM-EELS Experiment: All EELS spectra were acquired on a Nion aberration-corrected high-energy-resolution monochromated EELS-STEM (HERMES™) equipped with the Nion Iris Spectrometer,[54] operated at 30 kV with a convergence angle of 27 mrad and a collection angle of 25 mrad. All spectra were measured to have an energy resolution between 5.5 meV and 6.5 meV, as measured by the ZLP full-width at half-maximum. In all acquisitions, a power law background was used to fit the spectral regions directly before (120 meV – 140 meV) and after (220 meV –250 meV) the Rehstrahlen band, and then subtracted to remove contributions from the ZLP tail.

Acquisition details were as follows: The line profile in Figure 1 consisted of 150 spectra, with a calibration of 0.5 nm per pixel, a dispersion of 0.22 meV per spectrometer channel, and an acquisition time of 3 seconds per spectrum. The line profiles in Figure 2 and Figure 3 were both 2D spectrum images binned in the axis normal to the dispersive direction to create line profiles. For the bulk polariton measurement, a 9x192 pixel spectrum image was acquired and subsequently vertically binned across all nine pixels, with a calibration of 1.5625 nm per pixel, a

dispersion of 0.40 meV per spectrometer channel, and an acquisition time of 128 ms per pixel. For the edge polariton measurement, a 163x20 pixel spectrum image was acquired and binned across only the two pixels closest to the edge extending into the flake (region for binning shown in Figure S3). Including pixels in the edge of the flake for horizontal binning did not vary the measured dispersion significantly, and only had the effect of including small contributions from the LO phonon, which made the upper limit of the measured dispersion more difficult to quantify. The spectrum image had a calibration of 1.5703 nm per pixel, a dispersion of 0.40 meV per spectrometer channel, and an acquisition time of 500 ms per pixel. For Figure 3, a 50x50 pixels spectrum image was acquired with a calibration of 10 nm per pixel, a dispersion of 0.40 meV per spectrometer channel, and an acquisition time of 400 ms per pixel. For Figure 4, a 64x64 pixel spectrum image was acquired, with a calibration of 4 nm per pixel, a dispersion of 0.40 meV per spectrometer channel, and an acquisition time of 400 ms per pixels.

We have also included videos of the spectrum images for the bulk polariton, edge polariton, finite disk, and corner analyses, where a normalized 2D intensity is shown at frame-by-frame for all the energies in the Reststrahlen band (see Supporting Information).

The thickness of the flakes (18 nm in Figure 1, 12 nm in Fig. 2/3/5, and 8 nm in Fig. 4) were determined by comparing the experimental energy of the non-dispersive polariton peak to simulations, as we show in depth in Figure S12 in the Supporting Information.

Calibration and Validation of Datasets: Many factors can strongly influence the measured polariton dispersion, which need to be properly accounted for. In this analysis, we have included the specific pixel in the dataset deemed as the edge of the flake (a non-trivial assignment), the calibration of the spectrometer, which is difficult to carry out more accurately than around 1% at

the high dispersions used in monochromated EELS, and the reflection phase. We calibrated our measurements to the LO phonon at 200.1 meV in the BN flakes, the energy of which was not dependent on flake thickness or geometry. For the dataset in Figure 1, we found that a dispersion correction of 0.5% was needed. The datasets in Figure 2-5, which were all performed on the same day at the same dispersion, needed a dispersion correction of 1%. For the reflection phases and the edge pixel determination, which only applied to Figures 2 and 3, we compared to the simulated line profiles to determine the correct values. This calibration and selection process is shown in detail in the Supporting Discussion 2.

Simulations: All calculations were performed within the framework of classical macroscopic electrodynamics, which is known to reproduce very well the interaction of focused electron probes with optical excitations[55] in nanostructures such as those considered in this work. We used analytical expressions to calculate EELS spectra when dealing with an electron beam interacting with an infinite hBN slab. For more complex geometries (linear edge, corners, and disks), we used numerical solvers of the Poisson and Maxwell equations implemented in the commercial software Comsol Multiphysics. Further details on the formalism, analytical expressions, and models, as well as setting parameters for the numerical solvers, are described in the Supporting Discussion 3.

Supporting Information
Supporting Information is available from the Wiley Online Library or from the author.

Acknowledgements
Microscopy experiments conducted at the Center for Nanophase Materials Sciences, which is a DOE Office of Science User Facility using instrumentation within ORNL's Materials Characterization Core provided by UT-Battelle, LLC, under Contract No. DE-AC05-00OR22725 with the DOE and sponsored by the Laboratory Directed Research and

Development Program of Oak Ridge National Laboratory, managed by UT-Battelle, LLC, for the U.S. Department of Energy (JAH). AK and FJGA acknowledge support from the European Research Council (Advanced Grant No. 789104eNANO), the European Commission (Horizon 2020 Grants No. FET-Proactive 101017720-EBEAM and No. FET-Open 964591-SMART-electron), and the Spanish MINECO (SEV2015-0522). Support for hBN crystal growth from the Office of Naval Research (Award No. N00014-20-1-2474) is appreciated (JL and JHE).

Conflict of Interest

The Authors declare they have no conflict of interest.

References

[1] H. A. Atwater, A. Polman, *Nat. Mater.* **2010**, *9*, 205–213.
[2] F. Xia, H. Wang, D. Xiao, M. Dubey, A. Ramasubramaniam, *Nat. Photonics* **2014**, *8*, 899–907.
[3] F. Hu, Y. Luan, M. E. Scott, J. Yan, D. G. Mandrus, X. Xu, Z. Fei, *Nat. Photonics* **2017**, *11*, 356–360.
[4] F. Lu, M. Jin, M. A. Belkin, *Nat. Photonics* **2014**, *8*, 307–312.
[5] Z. Han, P. Lin, V. Singh, L. Kimerling, J. Hu, K. Richardson, A. Agarwal, D. T. H. Tan, *Appl. Phys. Lett.* **2016**, *108*, 141106.
[6] Y. Wu, Z. Hu, X.-T. Kong, J. C. Idrobo, A. G. Nixon, P. D. Rack, D. J. Masiello, J. P. Camden, *Phys. Rev. B* **2020**, *101*, 085409.
[7] A. Poddubny, I. Iorsh, P. Belov, Y. Kivshar, *Nat. Photonics* **2013**, *7*, 948–957.
[8] A. Nemilentsau, T. Low, G. Hanson, *Phys. Rev. Lett.* **2016**, *116*, 066804.
[9] S. Dai, Q. Ma, T. Andersen, A. S. Mcleod, Z. Fei, M. K. Liu, M. Wagner, K. Watanabe, T. Taniguchi, M. Thiemens, F. Keilmann, P. Jarillo-Herrero, M. M. Fogler, D. N. Basov, *Nat. Commun.* **2015**, *6*, 1–7.
[10] E. Yoxall, M. Schnell, A. Y. Nikitin, O. Txoperena, A. Woessner, M. B. Lundeberg, F. Casanova, L. E. Hueso, F. H. L. Koppens, R. Hillenbrand, *Nat. Photonics* **2015**, *9*, 674–678.
[11] D. N. Basov, M. M. Fogler, F. J. G. de Abajo, *Science* **2016**, *354*, DOI 10.1126/science.aag1992.
[12] M. Autore, P. Li, I. Dolado, F. J. Alfaro-Mozaz, R. Esteban, A. Atxabal, F. Casanova, L. E. Hueso, P. Alonso-González, J. Aizpurua, A. Y. Nikitin, S. Vélez, R. Hillenbrand, *Light Sci. Appl.* **2018**, *7*, 17172–17172.
[13] A. J. Giles, S. Dai, I. Vurgaftman, T. Hoffman, S. Liu, L. Lindsay, C. T. Ellis, N. Assefa, I. Chatzakis, T. L. Reinecke, J. G. Tischler, M. M. Fogler, J. H. Edgar, D. N. Basov, J. D. Caldwell, *Nat. Mater.* **2018**, *17*, 134–139.
[14] J. D. Caldwell, I. Aharonovich, G. Cassabois, J. H. Edgar, B. Gil, D. N. Basov, *Nat. Rev. Mater.* **2019**, *4*, 552–567.
[15] S. Dai, W. Fang, N. Rivera, Y. Stehle, B.-Y. Jiang, J. Shen, R. Y. Tay, C. J. Ciccarino, Q. Ma, D. Rodan-Legrain, P. Jarillo-Herrero, E. H. T. Teo, M. M. Fogler, P. Narang, J. Kong, D. N. Basov, *Adv. Mater.* **2019**, *31*, 1806603.
[16] S. Dai, Z. Fei, Q. Ma, A. S. Rodin, M. Wagner, A. S. McLeod, M. K. Liu, W. Gannett, W. Regan, K. Watanabe, T. Taniguchi, M. Thiemens, G. Dominguez, A. H. C. Neto, A. Zettl, F. Keilmann, P. Jarillo-Herrero, M. M. Fogler, D. N. Basov, *Science* **2014**, *343*, 1125–1129.

[17] J. D. Caldwell, L. Lindsay, V. Giannini, I. Vurgaftman, T. L. Reinecke, S. A. Maier, O. J. Glembocki, *Nanophotonics* **2015**, *4*, 44–68.
[18] Z. Yuan, R. Chen, P. Li, A. Y. Nikitin, R. Hillenbrand, X. Zhang, *ACS Photonics* **2020**, *7*, 2610–2617.
[19] S. Dai, Q. Ma, M. K. Liu, T. Andersen, Z. Fei, M. D. Goldflam, M. Wagner, K. Watanabe, T. Taniguchi, M. Thiemens, F. Keilmann, G. C. a. M. Janssen, S.-E. Zhu, P. Jarillo-Herrero, M. M. Fogler, D. N. Basov, *Nat. Nanotechnol.* **2015**, *10*, 682–686.
[20] L. V. Brown, M. Davanco, Z. Sun, A. Kretinin, Y. Chen, J. R. Matson, I. Vurgaftman, N. Sharac, A. J. Giles, M. M. Fogler, T. Taniguchi, K. Watanabe, K. S. Novoselov, S. A. Maier, A. Centrone, J. D. Caldwell, *Nano Lett.* **2018**, *18*, 1628–1636.
[21] P. Li, I. Dolado, F. J. Alfaro-Mozaz, F. Casanova, L. E. Hueso, S. Liu, J. H. Edgar, A. Y. Nikitin, S. Vélez, R. Hillenbrand, *Science* **2018**, *359*, 892–896.
[22] S. Dai, J. Zhang, Q. Ma, S. Kittiwatanakul, A. McLeod, X. Chen, S. G. Corder, K. Watanabe, T. Taniguchi, J. Lu, Q. Dai, P. Jarillo-Herrero, M. Liu, D. N. Basov, *Adv. Mater.* **2019**, *31*, 1900251.
[23] O. L. Krivanek, T. C. Lovejoy, N. Dellby, T. Aoki, R. W. Carpenter, P. Rez, E. Soignard, J. Zhu, P. E. Batson, M. J. Lagos, R. F. Egerton, P. A. Crozier, *Nature* **2014**, *514*, 209–212.
[24] J. A. Hachtel, A. R. Lupini, J. C. Idrobo, *Sci. Rep.* **2018**, *8*, 5637.
[25] N. Dellby, T. Lovejoy, G. Corbin, N. Johnson, R. Hayner, M. Hoffman, P. Hrncrik, B. Plotkin-Swing, D. Taylor, O. Krivanek, *Microsc. Microanal.* **2020**, *26*, 1804–1805.
[26] M. J. Lagos, A. Trügler, U. Hohenester, P. E. Batson, *Nature* **2017**, *543*, 529–532.
[27] H. Lourenço-Martins, M. Kociak, *Phys. Rev. X* **2017**, *7*, 041059.
[28] F. S. Hage, G. Radtke, D. M. Kepaptsoglou, M. Lazzeri, Q. M. Ramasse, *Science* **2020**, *367*, 1124–1127.
[29] X. Li, G. Haberfehlner, U. Hohenester, O. Stéphan, G. Kothleitner, M. Kociak, *Science* **2021**, *371*, 1364–1367.
[30] P. Rez, T. Aoki, K. March, D. Gur, O. L. Krivanek, N. Dellby, T. C. Lovejoy, S. G. Wolf, H. Cohen, *Nat. Commun.* **2016**, *7*, 10945.
[31] J. A. Hachtel, J. Huang, I. Popovs, S. Jansone-Popova, J. K. Keum, J. Jakowski, T. C. Lovejoy, N. Dellby, O. L. Krivanek, J. C. Idrobo, *Science* **2019**, *363*, 525–528.
[32] S. M. Collins, D. M. Kepaptsoglou, J. Hou, C. W. Ashling, G. Radtke, T. D. Bennett, P. A. Midgley, Q. M. Ramasse, *Nano Lett.* **2020**, *20*, 1272–1279.
[33] K. March, K. Venkatraman, C. D. Truong, D. Williams, P.-L. Chiu, P. Rez, *J. Microsc.* **2021**, *282*, 215–223.
[34] A. A. Govyadinov, A. Konečná, A. Chuvilin, S. Vélez, I. Dolado, A. Y. Nikitin, S. Lopatin, F. Casanova, L. E. Hueso, J. Aizpurua, R. Hillenbrand, *Nat. Commun.* **2017**, *8*, 95.
[35] W. Dong, R. Qi, T. Liu, Y. Li, N. Li, Z. Hua, Z. Gao, S. Zhang, K. Liu, J. Guo, P. Gao, *Adv. Mater.* **2020**, *32*, 2002014.
[36] N. Li, X. Guo, X. Yang, R. Qi, T. Qiao, Y. Li, R. Shi, Y. Li, K. Liu, Z. Xu, L. Liu, F. J. García de Abajo, Q. Dai, E.-G. Wang, P. Gao, *Nat. Mater.* **2021**, *20*, 43–48.
[37] G. Radtke, D. Taverna, N. Menguy, S. Pandolfi, A. Courac, Y. Le Godec, O. L. Krivanek, T. C. Lovejoy, *Phys. Rev. Lett.* **2019**, *123*, 256001.
[38] A. Konečná, T. Neuman, J. Aizpurua, R. Hillenbrand, *ACS Nano* **2018**, *12*, 4775–4786.
[39] A. B. Yankovich, B. Munkhbat, D. G. Baranov, J. Cuadra, E. Olsén, H. Lourenço-Martins, L. H. G. Tizei, M. Kociak, E. Olsson, T. Shegai, *Nano Lett.* **2019**, *19*, 8171–8181.

[40] L. H. G. Tizei, V. Mkhitaryan, H. Lourenço-Martins, L. Scarabelli, K. Watanabe, T. Taniguchi, M. Tencé, J.-D. Blazit, X. Li, A. Gloter, A. Zobelli, F.-P. Schmidt, L. M. Liz-Marzán, F. J. García de Abajo, O. Stéphan, M. Kociak, *Nano Lett.* **2020**, *20*, 2973–2979.
[41] D. T. Schoen, A. C. Atre, A. García-Etxarri, J. A. Dionne, M. L. Brongersma, *Nano Lett.* **2015**, *15*, 120–126.
[42] Y. Li, R. Qi, R. Shi, N. Li, P. Gao, *Sci. Bull.* **2020**, *65*, 820–826.
[43] M. Taleb, F. Davoodi, F. Diekmann, K. Rossnagel, N. Talebi, *ArXiv210101465 Cond-Mat Physicsphysics* **2021**.
[44] Y. Kurman, R. Dahan, H. H. Sheinfux, K. Wang, M. Yannai, Y. Adiv, O. Reinhardt, L. H. G. Tizei, S. Y. Woo, J. Li, J. H. Edgar, M. Kociak, F. H. L. Koppens, I. Kaminer, *Science* **2021**, *372*, 1181–1186.
[45] S. Mastel, A. A. Govyadinov, C. Maissen, A. Chuvilin, A. Berger, R. Hillenbrand, *ACS Photonics* **2018**, *5*, 3372–3378.
[46] P. Li, I. Dolado, F. J. Alfaro-Mozaz, A. Yu. Nikitin, F. Casanova, L. E. Hueso, S. Vélez, R. Hillenbrand, *Nano Lett.* **2017**, *17*, 228–235.
[47] P. A. Crozier, *Ultramicroscopy* **2017**, *180*, 104–114.
[48] J. A. Hachtel, J. R. Jokisaari, O. L. Krivanek, J. C. Idrobo, R. F. Klie, *Microsc. Today* **2021**, *29*, 36–41.
[49] T. G. Folland, A. Fali, S. T. White, J. R. Matson, S. Liu, N. A. Aghamiri, J. H. Edgar, R. F. Haglund, Y. Abate, J. D. Caldwell, *Nat. Commun.* **2018**, *9*, 1–7.
[50] A. Fali, S. T. White, T. G. Folland, M. He, N. A. Aghamiri, S. Liu, J. H. Edgar, J. D. Caldwell, R. F. Haglund, Y. Abate, *Nano Lett.* **2019**, *19*, 7725–7734.
[51] F.-P. Schmidt, H. Ditlbacher, U. Hohenester, A. Hohenau, F. Hofer, J. R. Krenn, *Nano Lett.* **2012**, *12*, 5780–5783.
[52] F. P. Schmidt, H. Ditlbacher, F. Hofer, J. R. Krenn, U. Hohenester, *Nano Lett.* **2014**, *14*, 4810–4815.
[53] J. Li, C. Elias, G. Ye, D. Evans, S. Liu, R. He, G. Cassabois, B. Gil, P. Valvin, B. Liu, J. H. Edgar, *J. Mater. Chem. C* **2020**, *8*, 9931–9935.
[54] O. L. Krivanek, T. C. Lovejoy, N. Dellby, R. W. Carpenter, *Microscopy* **2013**, *62*, 3–21.
[55] F. J. García de Abajo, *Rev. Mod. Phys.* **2010**, *82*, 209–275.